

High pressure synthesis, crystal structure and electronic properties of $Ba_3Hf(Se_{1-x}Te_x)5$ (x = 0-1)

Zelong Wang(王泽龙), Guodong Wang(王国东), Wenmin Li(李文敏), Runteng Cheng(陈润滕), Lei Duan(段磊), Jianfa Zhao(赵建发), Zheng Deng(邓正), Jianfeng Zhang(张建丰), Tingjiang Yan(颜廷江), Jun Zhang(张俊), Xiancheng Wang(望贤成), and Changqing Jin(靳常青)

Citation: Chin. Phys. B, 2025, 34 (**8**): 086101. DOI: 10.1088/1674-1056/adcea2
http://cpb.iphy.ac.cn; http://iopscience.iop.org/cpb

What follows is a list of articles you may be interested in

First-principles study of structural and electronic properties of multiferroic oxide Mn_3TeO_6 under high pressure

Xiao-Long Pan(潘小龙), Hao Wang(王豪), Lei Liu(柳雷), Xiang-Rong Chen(陈向荣), and Hua-Yun Geng(耿华运)
Chin. Phys. B, 2024, 33 (**7**): 076102. DOI: 10.1088/1674-1056/ad3ef6

First-principles study of a new BP_2 two-dimensional material

Zhizheng Gu(顾志政), Shuang Yu(于爽), Zhirong Xu(徐知荣), Qi Wang(王琪), Tianxiang Duan(段天祥), Xinxin Wang(王鑫鑫), Shijie Liu(刘世杰), Hui Wang(王辉), and Hui Du(杜慧)
Chin. Phys. B, 2022, 31 (**8**): 086107. DOI: 10.1088/1674-1056/ac5a40

Effect of heavy ion irradiation on the interface traps of AlGaN/GaN high electron mobility transistors

Zheng-Zhao Lin(林正兆), Ling Lü(吕玲), Xue-Feng Zheng(郑雪峰), Yan-Rong Cao(曹艳荣), Pei-Pei Hu(胡培培), Xin Fang(房鑫), and Xiao-Hua Ma(马晓华)
Chin. Phys. B, 2022, 31 (**3**): 036103. DOI: 10.1088/1674-1056/ac11e4

A new direct band gap silicon allotrope *o*-Si32

Xin-Chao Yang(杨鑫超), Qun Wei(魏群), Mei-Guang Zhang(张美光), Ming-Wei Hu(胡明玮), Lin-Qian Li(李林茜), and Xuan-Min Zhu(朱轩民)
Chin. Phys. B, 2022, 31 (**2**): 026104. DOI: 10.1088/1674-1056/ac11db

First-principles study of two new boron nitride structures: C12-BN and O16-BN

Hao Wang(王皓), Yaru Yin(殷亚茹), Xiong Yang(杨雄), Yanrui Guo(郭艳蕊), Ying Zhang(张颖), Huiyu Yan(严慧羽), Ying Wang(王莹), and Ping Huai(怀平)
Chin. Phys. B, 2022, 31 (**2**): 026102. DOI: 10.1088/1674-1056/ac0a69

SPECIAL TOPIC — Structures and properties of materials under high pressure

High pressure synthesis, crystal structure and electronic properties of $Ba_3Hf(Se_{1-x}Te_x)_5$ ($x = 0$–1)

Zelong Wang(王泽龙)[1,†], Guodong Wang(王国东)[2,†], Wenmin Li(李文敏)[3,†], Runteng Chen(陈润滕)[2], Lei Duan(段磊)[2], Jianfa Zhao(赵建发)[2,4], Zheng Deng(邓正)[2,4], Jianfeng Zhang(张建丰)[2,4,§], Tingjiang Yan(颜廷江)[1,¶], Jun Zhang(张俊)[2,4,‡], Xiancheng Wang(望贤成)[2,4], and Changqing Jin(靳常青)[2,4,♯]

[1] *Key Laboratory of Catalytic Conversion and Clean Energy in Universities of Shandong Province, School of Chemistry and Chemical Engineering, Qufu Normal University, Qufu* 273165, *China*

[2] *Beijing National Laboratory for Condensed Matter Physics, Institute of Physics, Chinese Academy of Sciences, Beijing* 100190, *China*

[3] *Institute of Quantum Materials and Physics, Henan Academy of Sciences, Zhengzhou* 450046, *China*

[4] *School of Physics, University of Chinese Academy of Sciences, Beijing* 100190, *China*

(Received 2 April 2025; revised manuscript received 11 April 2025; accepted manuscript online 21 April 2025)

Quasi one-dimensional polycrystalline samples of $Ba_3Hf(Se_{1-x}Te_x)_5$ ($x = 0$–1) are synthesized under high-temperature and high-pressure conditions. Using the powder x-ray diffraction technique and first-principles calculations, Ba_3HfSe_5 is identified as having a hexagonal structure with a space group of $P6_3/mcm$ (193) and lattice constants of $a = 9.5756(1)$ Å, $c = 6.3802(7)$ Å. The structure is composed of $Hf(Se_1)_6$ chains and Se_2 linear chains extending along the c-axis. As the doping content of Te increases, the lattice expands and leads to 5.8% and 7.3% increases of the a and c values and a 20.1% increase of the unit cell volume of Ba_3HfTe_5 compared to Ba_3HfSe_5. The detailed structural refinements show that the Hf vacancies decrease gradually as Te doping increases in the $Ba_3Hf(Se_{1-x}Te_x)_5$ ($x = 0$–1) materials, which leads to a decrease of electronic localization. In addition, the lower electronegativity of Te and the more extended orbitals with respect to Se contribute to orbital overlap between the inter chains. All these dominate the enhanced electron hopping, leading to a reduction of the bandgap from 1.95 eV to 0.23 eV for $Ba_3Hf(Se_{1-x}Te_x)_5$ ($x = 0$–1) materials as the Ba_3HfSe_5 evolves to Ba_3HfTe_5.

Keywords: high pressure synthesis, quasi one-dimensional structure, band gap, Te doping

PACS: 61.05.cp, 75.50.Lk, 61.66.Fn, 61.82.Fk

DOI: 10.1088/1674-1056/adcea2 **CSTR:** 32038.14.CPB.adcea2

1. Introduction

One-dimensional (1D) systems are often composed of 1D chain units. Due to this 1D structural characteristic, their electrical transport properties typically exhibit pronounced anisotropy along different crystal directions. For instance, in the 1D conductor $Li_{0.9}Mo_6O_{17}$,[1] electrons are able to move in the 1D zigzag chain of Mo–O–Mo along the b-axis. Conversely, there is a significant hindrance to electron transport between the interchains due to weak interactions. Based on electronic transport measurements, it was found that the average resistivities at 300 K for $Li_{0.9}Mo_6O_{17}$ single crystals along the b, c and a axes are ρ_b:ρ_c:$\rho_a \approx 1$:2.5:6.[2]

In a quasi 1D system, the electronic hopping between interchains has a significant influence on their electron transport properties. By enhancing the atomic orbital overlapping between interchains, changes in electronic transport behaviors and electronic structures are expected. Chemical doping provides an effective approach for regulating the interchain electron transitions and spin interactions in quasi 1D materials. For instance, quasi 1D $BaVS_3$ exhibits insulating behavior, accompanied by an incommensurate antiferromagnetic order transition.[3] By substituting sulfur with selenium, a metal-insulator transition is observed in $BaVSe_3$ due to the enhanced interchain coupling interactions.[4] $Ba_9Co_3Se_{15}$ undergoes a spin glass phase transition at 3 K[5] and the freezing temperature T_f of $Ba_9Co_3(Se_{1-x}S_x)_{15}$ gradually increases to 5.2 K with increasing sulfur doping content.[6] In addition, in 1D conductors, electron transport is easily disrupted due to the Umklapp scattering effect, which leads to a metal–insulator transition.[7,8] Also, electron back scattering or disorder induced by vacancies in the 1D system tends to localize the electrons, which further imposes important influences on the transport behavior.[9]

The quasi 1D Ba_3MX_5 (M = transition metal, X =

†These authors contributed equally to this work.
‡Corresponding author. E-mail: zhang@iphy.ac.cn
§Corresponding author. E-mail: zjf@iphy.ac.cn
¶Corresponding author. E-mail: tingjiangn@163.com
♯Corresponding author. E-mail: jin@iphy.ac.cn

© 2025 Chinese Physical Society and IOP Publishing Ltd. All rights, including for text and data mining, AI training, and similar technologies, are reserved.

chalcogen)[5,6,10–18] and Re_3MX_5 (Re = rare-earth metal, M = transition metal, X = pnictogen) have been extensively studied.[19–25] The quasi 1D structure is generally composed of face-sharing MX_6 octahedra chains along the 1D direction, which arrange into a triangular lattice within the *ab* plane. Re_3MX_5 usually adopts hexagonal space groups of $P6_3/mcm$ or $P6_3/mmc$. The MX_6 interchains are charge balanced by rare-earth ions with smaller ionic radii and higher oxidation states, which causes strong interchain coupling interactions and therefore all these materials are well-defined 3D conductors.[23,24] In Ba_3MX_5 systems, the interchains are separated by Ba ions. Because the coupling interaction between interchains is relatively weak, electronic hopping is prevented, and thus semiconductor behavior emerges.

In this work, quasi 1D Ba_3HfSe_5 was first synthesized as a model compound, and then Se was further substituted by Te to form the $Ba_3Hf(Se_{1-x}Te_x)_5$ ($x = 0$–1) polycrystalline sample. Then, detailed structural refinement was performed. Furthermore, ultraviolet–visible diffuse reflectance spectroscopy (UV–Vis DRS) and resistance measurements were used to measure the band gap of $Ba_3Hf(Se_{1-x}Te_x)_5$ materials. As the amount of Te doping increases in the $Ba_3Hf(Se_{1-x}Te_x)_5$ ($x = 0$–1) system, the band gaps monotonically decrease, which is related to the enhanced orbital overlapping between interchains and decreased electronic localization caused by the fewer Hf vacancies.

2. Experimental details

Polycrystalline samples of $Ba_3Hf(Se_{1-x}Te_x)_5$ ($x = 0$–1) were prepared by a high-pressure and high-temperature technique using a 6×1400 T cubic anvil high-pressure apparatus. Commercially available lumps of Ba (Alfa, immersed in oil, $> 99.2\%$ pure), crystalline powders of Hf (Alfa, 99.99% pure), Te (Alfa 99.99% pure) and Se (Alfa, 99.99% pure) were used as the starting materials. The precursor BaSe and BaTe were prepared in a vacuum quartz tube at 700 °C for 20 h. Then, BaSe (BaTe), Hf, and Se(Te) were finely ground at a stoichiometric ratio of 3:1:2, pressed into cylinders with a diameter of 6 mm and a height of 3 mm, and sintered at 1500 °C and 5 GPa for 30 min to obtain pure polycrystalline samples.

Powder x-ray diffraction (XRD) measurements were carried out on a Rigaku Smart Lab diffractometer with Cu $K\alpha$ radiation ($\lambda = 1.54059$ Å, 45 kV, 200 mA) in the 2θ range from 10° to 100° with a step size of 0.01°. The diffraction spectra were refined by Rietveld using GSAS and EXPGUI. The structural characteristics were analyzed by powder diffraction refinement and first-principles calculations. The magnetic properties were measured using a superconducting quantum interference device (SQUIDVSM; Quantum Design). The electronic transport properties were measured by four-probe electrical conductivity methods using a physical property measurement system. The band gaps were obtained by measuring the UV–Vis DRS based on the Tauc equation.

3. Results

Figure 1(a) shows the XRD patterns for the Ba_3HfSe_5 and Ba_3HfTe_5 samples, which show similar profiles to the previously discovered "315" Ba/Re_3MX_5 materials with a quasi 1D structure. Using Powder X software, the XRD patterns can be indexed as a hexagonal structure, mainly composed of face-sharing $HfSe/Te_6$ octahedral chains and Se/Te chains extending along the *c*-axis. In our previous research, a complex superlattice was found along 1D chains. For example, $Ba_6Cr_2S_{10}$[15] and $Ba_9Fe_3Se_{15}$[14] exhibit dimerized and trimerized superstructures along the *c*-axis, respectively, as solved by single crystal diffraction measurements. Here, further structural analysis could not discern the complex superstructure distortion within the $HfSe/Te_6$ octahedron chains. It is well known that 1D Fermi surfaces are prone to nesting due to the strong electron–phonon coupling, which leads to lattice instability and structural distortion along 1D direction.

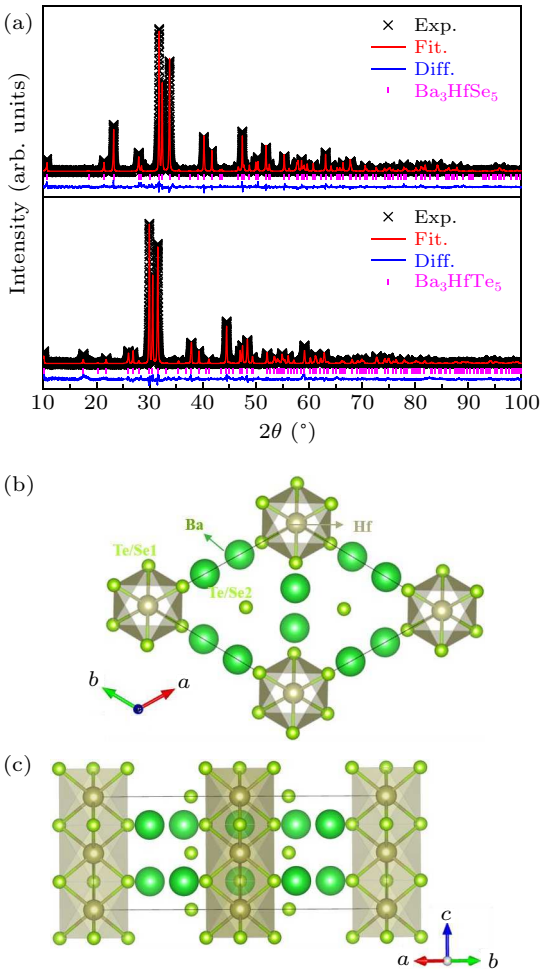


Fig. 1. (a) The typical XRD patterns and the refinement spectra for Ba_3HfSe_5 and Ba_3HfTe_5; (b) and (c) show the structural schemes for the $Ba_3Hf(Se_{1-x}Te_x)_5$ ($x = 0$–1) samples along directions [001] and [110], respectively.

Table 1. Crystallographic data for Ba_3HfSe_5 and Ba_3HfTe_5.

Crystallographic data for Ba_3HfSe_5						
Space group		$P6_3/mcm$ (193)				
Lattice parameters		$a = b = 9.5756(1)$ Å, $c = 6.3802(7)$ Å, $\alpha = \beta = 90°$, $\gamma = 120°$				
Unit-cell volume		506.64(5) Å^3				
Refinement parameters		$\chi^2 = 6.59$, $R_{wp} = 3.60\%$, $R_p = 2.50\%$				
Atom	x	y	z	Occ.	U (Å^2)	Wyck.
Ba	0.6168(2)	0	1/4	1	0.02(9)	6*g*
Hf	0	0	0	0.57(4)	0.02(4)	2*b*
Se_1	0.2310(6)	0	1/4	1	0.02(4)	6*g*
Se_2	1/3	2/3	0	1	0.04(7)	4*d*
Crystallographic data for Ba_3HfTe_5						
Space group		$P6_3/mcm$ (193)				
Lattice parameters		$a = b = 10.1293(4)$ Å, $c = 6.8467(8)$ Å, $\alpha = \beta = 90°$, $\gamma = 120°$				
Unit-cell volume		608.38(6) Å^3				
Refinement parameters		$\chi^2 = 5.20$, $R_{wp} = 3.71\%$, $R_p = 2.68\%$				
Atom	x	y	z	Occ.	U (Å^2)	Wyck.
Ba	0.6136(3)	0	1/4	1	0.03(6)	6*g*
Hf	0	0	0	0.80(7)	0.03(6)	2*b*
Te_1	0.2370(7)	0	1/4	1	0.02(5)	6*g*
Te_2	1/3	2/3	0	1	0.03(6)	4*d*

The nesting vector can quantitatively reflect the characteristic vector of the structural distortion. Therefore, the Fermi surface and phonon spectrum of the primitive cell of Ba_3HfSe_5 were analyzed through theoretical calculations to determine the dynamic stability of the material, and the accurate structure in the 1D direction was indirectly inferred. The theoretical calculation results indicate that the d_{z^2} orbital from the Hf atom and the p_z orbital from the intermediate Se atom cross the Fermi surface, proving that both the Se chains and the $HfSe_6$ chains are conductive chains, and there is no lattice instability in Ba_3HfSe_5. Therefore, Ba_3HfSe_5 exhibits a primitive cell along the *c*-axis, different from the dimer or trimer structures in $Ba_6Cr_2S_{10}$[15] and $Ba_9Fe_3Se_{15}$.[14] The detailed calculation results can be found in Fig. S1 in the supplemental materials.

Based on the structural analysis, the well-studied 1D Re_3MX_5 (RE = rare-earth metal, M = transition metal, X = pnictogen)[19–25] was used as a structural model to refine the XRD patterns of $Ba_3Hf(Se_{1-x}Te_x)_5$ (x = 0–1) samples. The refinement was performed according to the space group $P6_3/mcm$ (193). The typical XRD patterns and refinement spectra are shown in Figs. 1(a) and S2. The detailed crystallographic data are summarized in Tables 1 and S1–S4. The lattice constants of Ba_3HfSe_5 are $a = 9.5756(1)$ Å, $c = 6.3802(7)$ Å, and the unit cell volume is 506.64(5) Å^3. According to the refinement results, the crystal structure schemes of $Ba_3Hf(Se_{1-x}Te_x)_5$ (x = 0–1) were drawn, as shown in Figs. 1(b) and 1(c). The series of compounds adopt an inverse hexagonal Hf_5Sn_3Cu structure, composed of 1D $HfSe/Te_6$ chains and Se/Te chains. The $HfSe/Te_6$ chains form a triangular lattice in the *ab* plane and the distance between the chains is greater than 9.5 Å indicated by lattice constant a. Therefore, the $Ba_3Hf(Se_{1-x}Te_x)_5$ (x = 0–1) samples exhibit well-defined 1D structural characteristics. Along the $Hf(Se_1/Te_1)_6$ 1D chains, Hf atoms locate at the (0, 0, 0) site coordinated by Se/Te_1 atoms, where the occupation of Hf is 57.4%. The Se_2/Te_2 atoms form 1D chains along the *c*-axis located in the center of the triangular lattice.

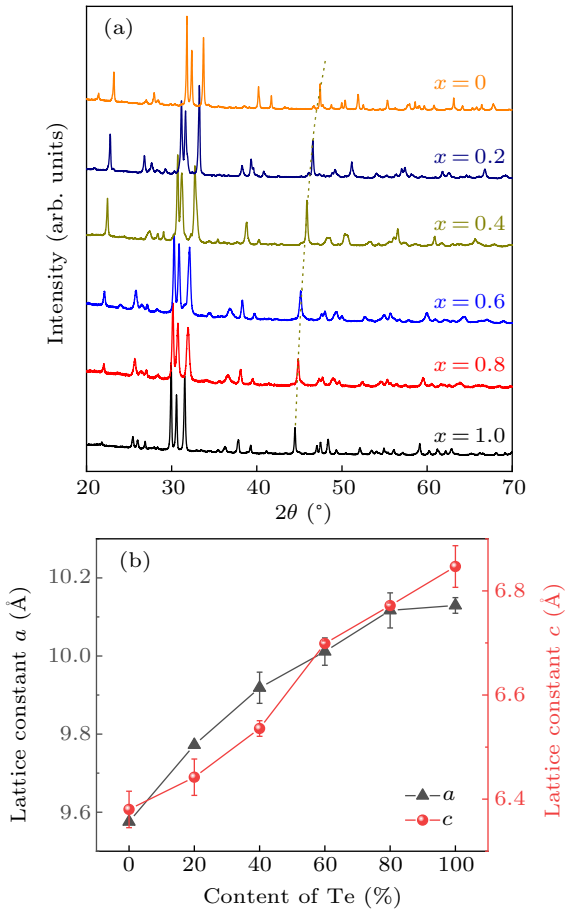


Fig. 2. (a) XRD patterns and (b) the doping content of Te dependence of the lattice constants of $Ba_3Hf(Se_{1-x}Te_x)_5$ (x = 0–1) samples.

With complete substitution of Se by Te, the $Ba_3Hf(Se_{1-x}Te_x)_5$ (x = 0–1) polycrystalline samples were synthesized under high-pressure and high-temperature conditions. The XRD patterns collected at room temperature are shown in Fig. 2(a). It is evident that the diffraction peaks gradually shift towards lower angles as Te doping increases, which indicates that the lattice expansion occurs. The systematic shift also proves the successful doping of Te in $Ba_3Hf(Se_{1-x}Te_x)_5$ (x = 0–1) samples. After careful analysis of the structural parameters, it is found that Te preferentially occupies the Se_2 sites and then Se_1 sites; the occupation of Hf increases as the Te content increases. The detailed occupation information is summarized in Table 2. Complete substitution of Se by Te leads to the formation of pure Ba_3HfTe_5, where the lattice constants are $a = 10.1293(4)$ Å and $c = 6.8467(8)$ Å and the occupation of Hf is 80.7%. In Figs. 2(b) and S3, for the $Ba_3Hf(Se_{1-x}Te_x)_5$ (x = 0–1) system, the lattice constants

a and c, as well as the unit cell volume (V), increase monotonically with the increase in Te doping amount (x). Compared with Ba_3HfSe_5, the unit cell volume of Ba_3HfTe_5 expands by approximately 20.1%. Figure 2(b) shows a non-ideal linear relationship between the Te content and the lattice constants. As the Te doping increases, it is found that the Hf vacancies decrease in the $Ba_3Hf(Se_{1-x}Te_x)_5$ samples, which may exert some influence on the changes in lattice parameters. For instance, Ba_3HfTe_5 with $\sim 80\%$ Hf occupation shows a unit cell volume deviating from the linear relationship shown in Fig. S3. Additionally, there may be some non-uniformity in the samples prepared under high-pressure conditions, which also contributes to the nonlinear changes in lattice parameters.

Table 2. The occupancy of Se, Te, and Hf atoms in $Ba_3Hf(Se_{1-x}Te_x)_5$ ($x = 0$–1) from the XRD refinement.

$Ba_3Hf(Se_{1-x}Te_x)_5$ ($x = 0$–1)						
x	0	0.2	0.4	0.6	0.8	1
Se_1	1	0.97(6)	0.88(5)	0.64(5)	0.34(3)	0
Te_1	0	0.02(4)	0.11(5)	0.35(5)	0.65(7)	1
Se_2	1	0.67(6)	0.29(5)	0.05(1)	0.03(9)	0
Te_2	0	0.32(4)	0.70(5)	0.94(9)	0.96(1)	1
Hf	0.57(4)	0.61(3)	0.63(5)	0.69(3)	0.71(6)	0.80(7)

Due to the difference in electronegativity, the Te doping exerts important influence on the electronic transport behaviors in the $Ba_3Hf(Se_{1-x}Te_x)_5$ ($x = 0$–1) samples. Figure 3(a) shows the temperature dependence of resistance for Ba_3HfSe_5. The resistance increases as the temperature decreases, exhibiting a semiconducting behavior. The inset presents the linear fit of $\ln(R)$ to inverse temperature, using $\rho \propto \exp\left(E_g/2k_BT\right)$, where E_g is the semiconducting band gap and k_B is Boltzmann's constant. The resistivity curve can be well fitted, and the E_g of $Ba_3Hf(Se_{1-x}Te_x)_5$ ($x = 1$) is estimated to be 0.23 eV. Similar methods were used to obtain the band gaps of $Ba_3Hf(Se_{1-x}Te_x)_5$ ($x = 0.8$, 0.6), which were estimated to be 0.89 eV and 0.97 eV, respectively, as shown in Fig. S4(a). The resistance of $Ba_3Hf(Se_{1-x}Te_x)_5$ ($x = 0$–0.4) is beyond the range of measurement by four-terminal sensing. Therefore, UV-Vis DRS was used to analyze the optical properties of $Ba_3Hf(Se_{1-x}Te_x)_5$ ($x = 0$–0.4). The Tauc equation was used to fit their band gaps, $(\alpha h\nu)^n = A\left(h\nu - E_g\right)$, where α is the energy-dependent absorption coefficient, h is the Planck constant, ν is the photon frequency, E_g is the band gap energy, and A is a constant. The n factor depends on the nature of the electron transition and is equal to 1/2 or 2 for the indirect and direct transition band gaps, respectively. The band gaps of $Ba_3Hf(Se_{1-x}Te_x)_5$ ($x = 0$–0.4) were estimated based on the assumption that n equals 2 for the semiconductor with a direct band gap, and the results are shown in Figs. 3(b) and S4(b). The band gaps show obvious decreases, ranging from 1.95 eV to 0.23 eV as the doping content of Te increases. The results of the magnetic susceptibility measurements indicate that Ba_3HfSe_5 and Ba_3HfTe_5 exhibit significant diamagnetism within the measured temperature range of 2–300 K and applied magnetic field of 500 Oe, as depicted in Fig. S5.

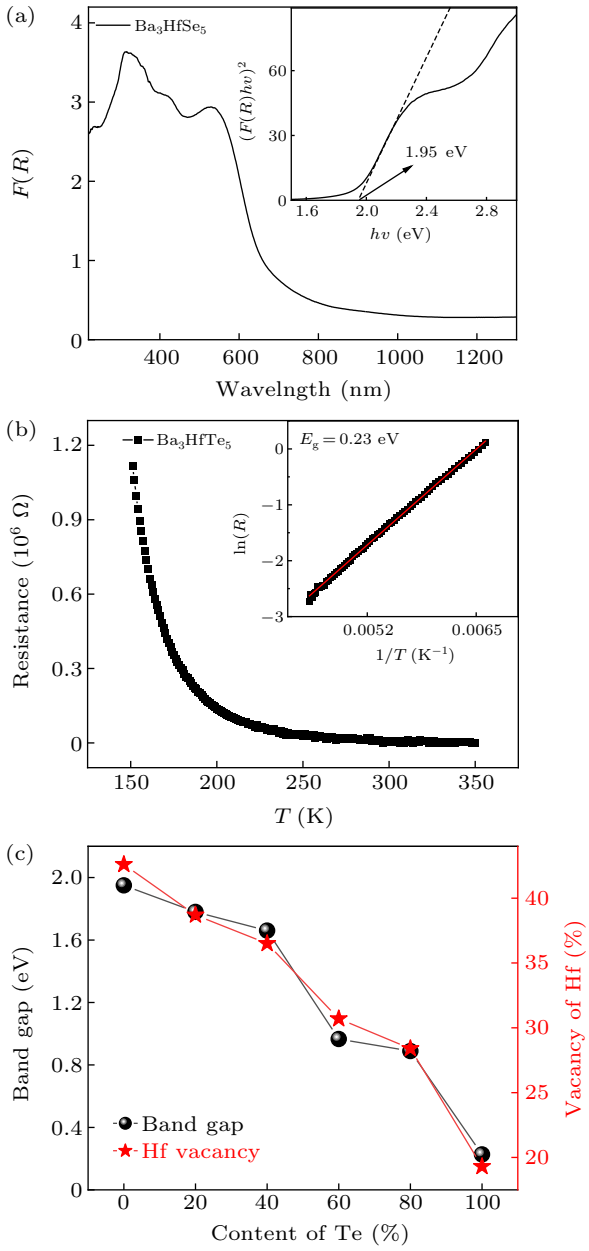


Fig. 3. (a) UV–Vis diffuse reflectance spectra of Ba_3HfSe_5; (b) the resistance as a function of temperature for the Ba_3HfTe_5 sample and the inset shows the inverse temperature dependence of $\ln(R)$; (c) the Te doping content dependence of energy bandgap and vacancies of Hf for $Ba_3Hf(Se_{1-x}Te_x)_5$ ($x = 0$–1) samples.

4. Discussion

According to the theoretical calculations, an ideal Ba_3HfSe_5 crystal should be a 1D conductor, in which the d_{z^2} orbital from the Hf atom and the p_z orbital from the intermediate Se atom cross the Fermi surface. Thus, both Se chains and $HfSe_6$ chains are conductive chains. Nevertheless, the electrical transport behavior along the 1D direction is likely to be disrupted due to Umklapp scattering, which often affects electron migration along 1D chains and leads to the emergence

of a correlation energy gap.[7,8] Therefore, Ba_3HfSe_5 shows semiconducting behavior in this work.

In the $Ba_3Hf(Se_{1-x}Te_x)_5$ ($x = 0$–1) system, Te atoms preferentially occupy the Se_1 site in the $HfSe_6$ chains and then the Se_2 site in the Se chains. Compared with Se, the Te atom, with its larger radius, has weaker electronegativity due to the more extended orbitals, which also contribute to the increase in lattice parameters and the larger distance between interchains as the doping content increases. In the 1D chain system, the interchain electron hopping plays a vital role in the electronic transport behaviors. As the amount of Te increases in the $Ba_3Hf(Se_{1-x}Te_x)_5$ ($x = 0$–1) system, more orbital overlap occurs between the interchains due to the more extended orbitals of the Te atoms. Therefore, electron hopping between the interchains should be easier, despite of the larger distances as the Te content increases.

In addition, with an increase of Te doping amount, the Hf vacancies decrease significantly in the $Ba_3Hf(Se_{1-x}Te_x)_5$ ($x = 0$–1) system. It is well known that the vacancies in 1D materials can localize electrons and decrease electron transport. Compared with Ba_3HfSe_5 with more than 40% Hf vacancies, Ba_3HfTe_5 only exhibits Hf vacancies of approximately 20%. Thus, the fewer Hf vacancies in the $Ba_3Hf(Se_{1-x}Te_x)_5$ ($x = 0$–1) system contributes to enhanced electronic hopping. Therefore, the bandgap evolution in the $Ba_3Hf(Se_{1-x}Te_x)_5$ ($x = 0$–1) system mainly derives from the contributions of Hf vacancies and Te doping.

5. Conclusion

The 1D $Ba_3Hf(Se_{1-x}Te_x)_5$ ($x = 0$–1) materials were synthesized under high temperature and high pressure, in which Se could be completely substituted by Te. These materials exhibit a hexagonal structure with uniformly spaced Hf atoms along the 1D $HfSe/Te_6$ chains and Se/Te linear chains. As the Te doping increases, the Hf vacancies gradually decrease from 40% to 20%, and the interchain interactions increase due to the more extended orbitals of Te, which contributes to electron delocalization and enhanced hopping between interchains. All this results in a reduction of the band gap.

Acknowledgments

Project supported by the National Key R&D Program of China (Grant Nos. 2023YFA1406001 and 2024YFA1408004) and the National Natural Science Foundation of China (Grant Nos. 12104488 and 12474097).

References

[1] Dos Santos C A M, White B D, Yu Y K, Neumeier J J and Souza J A 2007 *Phys. Rev. Lett.* **98** 266405
[2] Da Luz M S, Dos Santos C A M, Moreno J, White B D and Neumeier J J 2007 *Phys. Rev. B* **76** 233105
[3] Nakamura H, Yamasaki T, Giri S, Imai H, Shiga M, Kojima K, Nishi M, Kakurai K and Metoki N 2000 *J. Phys. Soc. Jpn.* **69** 2763
[4] Akrap A, Stevanović V, Herak M, Miljak M, Barišić N, Berger H and Forró L 2008 *Phys. Rev. B* **78** 235111
[5] Duan L, Wang X C, Zhang J, Zhao J F, Cao L P, Li W M, Yu R Z, Deng Z and Jin C Q 2020 *Chin. Phys. B* **29** 036102
[6] Duan L, Wang X C, Zhang J, Zhao J F, Li W M, Cao L P, Zhao Z W, Xiao C, Ren Y, Wang S, Zhu J and Jin C Q 2021 *Chin. Phys. B* **30** 106101
[7] Giamarchi T 1991 *Phys. Rev. B* **44** 2905
[8] Vescoli V, Degiorgi L, Henderson W, Grüner G, Starkey K P and Montgomery L K 1998 *Science* **281** 1181
[9] Zhang J, Su R, Wang X C, Li W M, Zhao J F, Deng Z, Zhang S J, Feng S M, Liu Q Q, Zhao H Z, Guan P F and Jin C Q 2017 *Inorg. Chem. Front.* **4** 1337
[10] Zhang J, Jia Y T, Wang X C, Li Z, Duan L, Li W M, Zhao J F, Cao L P, Dai G Y, Deng Z, Zhang S J, Feng S M, Yu R Z, Liu Q Q, Hu J P, Zhu J L and Jin C Q 2019 *NPG Asia Mater.* **11** 60
[11] Almoussawi B, Tomohiri H, Kageyama H and Kabbour H 2021 *Eur. J. Inorg. Chem.* **2021** 1271
[12] Zhang J, Liu M, Wang X C, Zhao K, Duan L, Li W M, Zhao J F, Cao L P, Dai G Y, Deng Z, Feng S M, Zhang S J, Liu Q Q, Yang Y F and Jin C Q 2018 *J. Phys. Condens. Matter* **30** 214001
[13] Zhang J, Zhang X Y, Xia Y H, Zhao J F, Duan L, Wang G, Min B, Cao H, Dela Cruz C R, Zhao K, Sun H, Zhu J, Zhang J, Xiang T, Wang X and Jin C 2023 *Phys. Rev. B* **108** 174423
[14] Zhang J, Komarek A C, Jin M, *et al.* 2021 *Phys. Rev. Mater* **5** 054606
[15] Zhang J, Wang X C, Zhou L, *et al.* 2022 *Adv. Mater.* **34** 2106728
[16] Duan L, Chen X M, Wang Z L, Wei Y T, Zhang J, Feng Y G, Wang S, Du S X, Zhao Z W, Xiao C J, Wang X C and Jin C Q 2024 *J. Alloys Compd.* **1007** 176496
[17] Zhang J, Duan L, Wang Z, Wang X C, Zhao J F, Jin M L, Li W M, Zhang C L, Cao L P, Deng Z, Hu Z W, Agrestini S, Valvidares M, Lin H J, Chen C T, Zhu J L and Jin C Q 2020 *Inorg. Chem.* **59** 5377
[18] Zhang J, Jin M L, Li X, Wang X C, Zhao J F, Liu Y, Duan L, Li W M, Cao L P, Chen B J, Wang L J, Sun F, Wang Y G, Yang L X, Xiao Y M, Deng Z, Feng S M, Jin C Q and Zhu J L 2020 *Chin. Phys. Lett.* **37** 087106
[19] Bollore G, Ferguson M J, Hushagen R W and Mar A 1995 *Chem. Mat.* **7** 2229
[20] Ferguson M J, Hushagen R W and Mar A 1997 *J. Alloys Compd.* **249** 191
[21] Murakami T, Yamamoto T, Takeiri F, Nakano K and Kageyama H 2017 *Inorg. Chem.* **56** 5041
[22] Duan L, Zhang J, Wang X C, Zhao J F, Cao L P, Li W M, Deng Z, Yu R Z, Li Z and Jin C Q 2020 *J. Alloys Compd.* **831** 154697
[23] Duan L, Wang X C, Zhan F Y, Zhang J, Hu Z W, Zhao J F, Li W M, Cao L P, Deng Z, Yu R Z, Lin H J, Chen C T, Wang R and Jin C Q 2020 *Sci. China Mater.* **63** 1750
[24] Duan L, Wang X C, Zhang J, Hu Z, Zhao J F, Feng Y G, Zhang H L, Lin H J, Chen C T, Wu W, Li Z, Wang R, Zhang J F, Xiang T and Jin C Q 2022 *Phys. Rev. B* **106** 184405
[25] Duan L, Wang X C, Zhang J, Zhao J F, Zhao Z W, Xiao C J, Guan C L, Wang S, Shi L P, Zhu J L and Jin C Q 2022 *J. Alloys Compd.* **905** 164214